A Partial Element Equivalent Circuit Model of a Permanent Magnet Electrodynamic Suspension

1st Louis Beauloye
Institute of Mechanics, Materials and Civil Engineering
UCLouvain
Louvain-La-Neuve, Belgium
louis.beauloye@uclouvain.be

2nd Bruno Dehez
Institute of Mechanics, Materials and Civil Engineering
UCLouvain
Louvain-La-Neuve, Belgium
bruno.dehez@uclouvain.be

***Abstract*—Permanent magnet electrodynamic suspensions rely on induced currents for the magnetic levitation of transportation systems. To predict these currents and the forces they generate, a partial element equivalent circuit model is presented in this paper. By discretizing the conductive track into a network of interconnected elements, the model is able to compute complex patterns of eddy currents and consider the skin effect. Suspensions with both bulk and perforated conductors are modeled with an error below 3% compared to precise references and with a significantly reduced computational cost compared to time-dependent finite element simulations. Experimental measurements further validate the predictions of the model. Additionally, the model is also adapted to study the vertical dynamics of the suspension, without using additional finite element identifications, and confirmed its unstable behavior.**

***Index Terms*—PEEC, electrodynamic suspension, PM-EDS, model**

I. Introduction

Electrodynamic suspensions (EDSs) can assure the magnetic levitation (MAGLEV) of high-speed transportation systems. They consist of a magnetic field source moving relatively to a conductive track, and inducing eddy currents that in turn react with the source to produce two main components of forces. The lift force enables the vehicle to levitate, whereas the drag force opposes its motion. Permanent magnets (PMs) constitute a simple and cost-effective solution for the EDS, known therefore as PM-EDS [1].

The forces generated by PM-EDSs are often computed using analytical models based on the resolution of Maxwell's equations in quasi-static conditions [2], [3]. These models offer a good trade-off between accuracy and computation time. However, these approaches are limited to suspensions involving bulk conductors and PMs experiencing either constant or null longitudinal and vertical velocities.

Discrete tracks, made of either conductive loops or perforated conductors, can potentially have better performance indicators, e.g. lift-to-drag ratio, compared to bulk conductors [1], [4]. Such tracks can be modeled using magnetically coupled equivalent circuits involving lumped parameters [4]–[7]. Although fast and accurate, these methods are limited to tracks in which the main induced current flow is uniformly distributed and known in advance [8]. This therefore neglects the skin effect and the locally induced eddy currents.

The vertical dynamic behavior of the electrodynamic suspension can be crucial to study [9]. Several approaches have been studied so far. The simplest involves deriving equivalent parameters, such as stiffness or damping [10], [11], but this has been shown to be insufficient for capturing the full behavior of the suspension [12]. Equivalent circuits models can also simulate the dynamics of the system by coupling electrical and mechanical equations [12], [13]. However, these equivalent circuits rely on lumped parameters that must be identified through simulations using finite element methods (FEM).

Both discrete tracks and vertical dynamics can be modeled using time-dependent FEM but at the expense of significant computational cost, preventing in-depth analyses and optimizations. An alternative is to discretize the conductive material into interconnected partial elements, forming equivalent electrical circuits in which the eddy currents are computed. The partial element equivalent circuits (PEEC) method [14], [15] has been applied to eddy current problems involving moving objects [16], [17], demonstrating its potential for this application. However, these analyses were not specifically applied to PM-EDS, nor did they investigated perforated conductors. They were also not adapted for studying the vertical dynamics of the suspension.

In this context, this paper presents a PEEC model to study permanent magnet electrodynamic suspensions in both quasi-static and dynamic conditions, without requiring additional FEM simulations. This model accounts for the complex patterns of eddy currents locally induced in bulk conductors, whether perforated or not. The PM-EDS is firstly presented and followed by the general assumptions of the model and the discretization it introduces. The steady-state model is then described along side both its numerical and experimental validation. Finally, the dynamical model is explained and used for a simple dynamical study.

II. General considerations

Before developing the actual models, details common to both steady-state and dynamic models are discussed. This starts with the case study for their application, and then moves on to the assumptions and the discretization introduced.

L. Beauloye is a Research Fellow of the Fonds de la Recherche Scientifique - FNRS

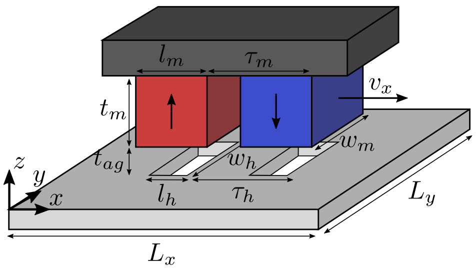

Fig. 1. Case study with a perforated track for the application of the PEEC model.

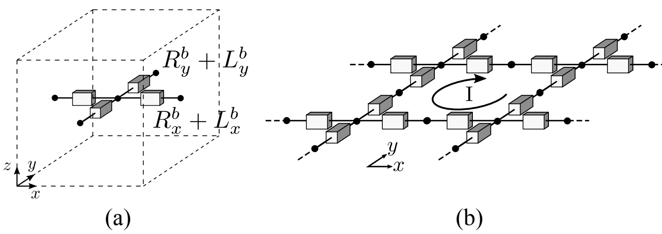

Fig. 2. (a) Partial conductive element. (b) Current loop formed by the connection of four elements.

A. Case study

The present model is applied to a permanent magnet electrodynamic suspension, depicted in Fig. 1 with its associated parameters. As shown, the conductive track can be perforated, when both l_h and w_h are different from zero. The motion direction is along the x-axis while the levitation direction is along the z-axis.

B. Assumptions

The PEEC model is based on the following assumptions:

- The model is periodic in the x-direction. The magnetic field source is computed from a Fourier-based model and therefore needs to be periodic. For the track, this is not a requirement but it enables the reduction of the number of degrees of freedom (DoFs), directly related to the dimensions of the numerical system to solve. The period is chosen to be equal to the wavelength of the PMs ($L_x = 2\tau_m$).
- The back-iron, closing the PM flux lines, is perfect with an infinite magnetic permeability.
- The eddy currents in the z-direction are neglected, as in [18]. This is not necessary for deriving the model, but it helps reduce its complexity. The validity of that hypothesis will be tested on perforated tracks in Section III-B.
- The longitudinal speed is constant.
- The impact of the ferromagnetic back-iron on the eddy current reaction field is neglected.

C. Discretization

The conductive track is discretized into parallelepidal conductive elements shown in Fig. 2(a). These elements have four branches in the xy-plane, each consisting of a series connection of a resistance and an inductance, which are connected to a central potential node and to the adjacent elements. The elements are not connected in the z-direction since the vertical component of the current is neglected. However, the discretization in that direction is still needed to capture the skin effect. As a first approach, we assumed that all the elements have the same dimensions. The branch resistances can then be expressed as:

$$R_{x,k}^b = \rho_k \frac{l_x^b}{S_{yz}} = \rho_k \frac{L_x N_y N_z}{N_x L_y L_z} \tag{1}$$

$$R_{y,k}^b = \rho_k \frac{l_y^b}{S_{xz}} = \rho_k \frac{L_y N_x N_z}{N_y L_x L_z} \tag{2}$$

where ρ_k is the resistivity of element k, S_{yz} and S_{xz} are the cross-sections of the elements in the yz- and xz-planes respectively, l_x^b and l_y^b are the lengths of branches in the x- and y- directions, and N_x, N_y, N_z are the numbers of elements in all three directions. The branch partial self and mutual inductances are computed using partial inductance formulae of bar conductors from [19]. These formulae are very precise but rather complex to evaluate. In an effort to reduce the computation time, when the distance between bar conductors is sufficient, their mutual inductance can be approximated, using filament conductors, thanks to the formulae provided by Grover [20] and Neumann's formula, as used in [21].

III. Steady-state model

This section first describes the steady-state PEEC model, considering a constant longitudinal speed of the suspension and no vertical speed. It is then validated when compared to analytical and FEM simulations, without and with holes in the conductive plate. Experimental measurements are also compared to the predictions of the model.

A. Derivation

Four blocks form a loop, illustrated in Fig. 2(b), in which Faraday's law can be applied. By decomposing the quantities in harmonic components, Faraday's laws in all the loops can be written, in the frequency domain, as:

$$\sum_{n=1}^{N} \mathbf{\Lambda} \left(\mathbf{R} + j\omega_n \mathbf{L} \right) \mathbf{\Lambda}^T \mathbf{I}_n = -v_x \sum_{n=1}^{N} \frac{\partial \boldsymbol{\varphi}_n}{\partial x} \tag{3}$$

with $\mathbf{\Lambda}$ an incidence matrix linking the branch to the loop quantities, $\mathbf{I}_n$ the n-th harmonic of the loop current vector, $\boldsymbol{\varphi}_n$ the n-th harmonic of the magnetic flux vector due to the PMs intercepted by the loop, $\omega_n = n\pi/\tau_m$ and:

$$\mathbf{R} = \begin{bmatrix} \mathbf{R}_x^B & \mathbf{0} \\ \mathbf{0} & \mathbf{R}_y^B \end{bmatrix} \tag{4}$$

$$\mathbf{R}_x^B = \begin{bmatrix} R_{x,0}^B & \cdots & 0 \\ \vdots & \ddots & \vdots \\ 0 & \cdots & R_{x,N_b-1}^B \end{bmatrix} \tag{5}$$

$$\mathbf{R}_y^B = \begin{bmatrix} R_{y,0}^B & \cdots & 0 \\ \vdots & \ddots & \vdots \\ 0 & \cdots & R_{y,N_b-1}^B \end{bmatrix} \tag{6}$$

$$\mathbf{L} = \begin{bmatrix} \mathbf{L}_x^B & \mathbf{0} \\ \mathbf{0} & \mathbf{L}_y^B \end{bmatrix} \tag{7}$$

$$\mathbf{L}_x^B = \begin{bmatrix} L_{x,0}^{B,e} & \cdots & M_{x,0(N_b-1)}^{B,e} \\ \vdots & \ddots & \vdots \\ M_{x,(N_b-1)0}^{B,e} & \cdots & L_{x,N_b-1}^{B,e} \end{bmatrix} \tag{8}$$

$$\mathbf{L}_y^B = \begin{bmatrix} L_{y,0}^{B,e} & \cdots & M_{y,0(N_b-1)}^{B,e} \\ \vdots & \ddots & \vdots \\ M_{y,(N_b-1)0}^{B,e} & \cdots & L_{y,N_b-1}^{B,e} \end{bmatrix} \tag{9}$$

The superscript B denotes the series connection of two branch elements. N_b is the total number of branches. Equivalent inductances $L_k^{B,e}$ and $M_{ik}^{B,e}$ are used in the matrices, as in [22]. Since the domain is periodic in the x-direction, currents that are an integer number of periods apart are equal. Only one period can therefore be studied with the contribution of all the other ones being integrated into an equivalent inductance:

$$L_k^{B,e} = L_k^B + \sum_{p=1}^{P} M_{k(k+p(N_b-1))}^B \tag{10}$$

$$M_{ik}^{B,e} = M_{ik}^B + \sum_{p=1}^{P} M_{i(k+p(N_b-1))}^B \tag{11}$$

where P denotes the number of periods impacting the main period of interest. The periodicity is also taken into account in the construction of the incidence matrix $\mathbf{\Lambda}$.

The magnetic flux φ_n intercepted by one loop due to the PM arrangement is equal to:

$$\varphi_n = \int_{S_{loop}} \sum_m C_{nm} e^{\alpha_{nm} z_{loop}} e^{j\frac{2n\pi x}{L_x}} e^{j\frac{2m\pi y}{L_y}} dS \tag{12}$$

where S_{loop} is the area of the loop, z_{loop} is the z-coordinate of the loop and $\alpha_{nm} = \sqrt{\frac{2n\pi}{L_x}^2 + \frac{2m\pi}{L_y}^2}$. The coefficient C_{nm} is computed from a Fourier-based model. For the present case study, C_{nm} is equal to:

$$C_{nm} = \frac{B_r}{nm\pi^2}\left(1 - e^{-2\alpha_{nm}t_m}\right)\sin\left(\frac{n\pi l_m}{2\tau_m}\right) \\ \sin\left(\frac{m\pi w_m}{2L_y}\right)\left(1-\cos\left(n\pi\right)\right)\left(1-\cos\left(m\pi\right)\right) \tag{13}$$

The system of equations (3) can be solved numerically. Once all the currents are known, the mean electromagnetic force is calculated in the following way:

$$\mathbf{F}_{mean} = \sum_n \mathrm{Re}\left[\frac{1}{2}\mathbf{I_n}^T \frac{\partial \boldsymbol{\varphi_n}}{\partial \mathbf{x}}^*\right] \tag{14}$$

TABLE I
PARAMETERS OF THE CASE STUDY FOR THE VALIDATION OF THE PEEC MODEL

Parameter	Symbol	Value	Unit
Air gap thickness	t_{ag}	5	mm
Track thickness	t_c	10	mm
Track conductivity	σ_c	3.5e7	S/m
Track width	L_y	100	mm
Track length	L_x	60	mm
Track pitch	τ_c	30	mm
Track hole length	l_h	15	mm
Track hole width	w_h	20	mm
PM thickness	t_m	20	mm
PM length	l_m	20	mm
PM width	w_m	20	mm
PM pole pitch	τ_m	30	mm
Back-iron thickness	t_{ir}	5	mm
Back-iron length	l_{ir}	50	mm
Back-iron width	w_{ir}	20	mm
Gap length	l_g	10	mm
PM remanence	B_r	1.4	T
PM permeability	$\mu_{r,m}$	1	-
Back-iron permeability	$\mu_{r,ir}$	1000	-
Translational speed	v_x	50	m/s

The spatial evolution of the forces with the position of the PMs x_{PM} can be expressed as:

$$\mathbf{F}_{sp}(x_{\mathrm{PM}}) = \mathrm{Re}\left[\sum_n \mathbf{I_n}(x_{\mathrm{PM}})^T\right] \mathrm{Re}\left[\sum_n \frac{\partial \boldsymbol{\varphi_n}}{\partial \mathbf{x}}(x_{\mathrm{PM}})\right] \tag{15}$$

B. Numerical validation

The PEEC model, being periodic along the x-axis, must therefore be validated against an accurate periodic reference but fast enough to easily vary parameters such as the speed. A 3-D analytical model, such as described in [23], is used for this purpose. The forces in the continuous track computed by the PEEC model are compared to the analytical reference in Fig. 3, for different numbers of elements in the z-direction, while keeping 20 elements in each of the other directions. Since the skin depth decreases with the speed, it is observed that more elements are needed to accurately model the suspension at higher speeds. For the finest discretization, the relative error remains below 0.7 % for all speeds, demonstrating the accuracy of the model and its underlying assumptions.

In Fig. 4, the number of elements is varied in both x- and y-directions while keeping $N_z = 5$. The reference is taken to be the PEEC model with the finest discretization. The figure shows the convergence of the model as the discretization increases, though at the expense of longer computation time. A 99 % convergence is achieved for a computation time of approximately 10 s.

One of the significant advantages of the PEEC model is its ability to consider holes in the track. A comparison between

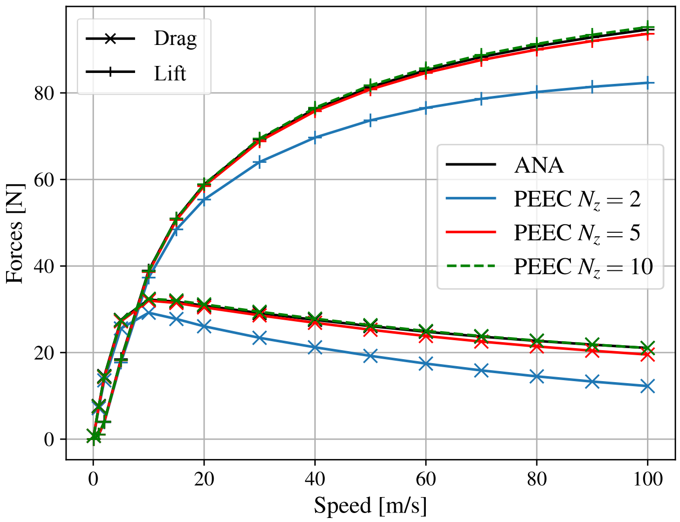

Fig. 3. Comparison of the evolution of the forces with the speed computed with an analytical model and the PEEC model for three different discretizations along the z-axis.

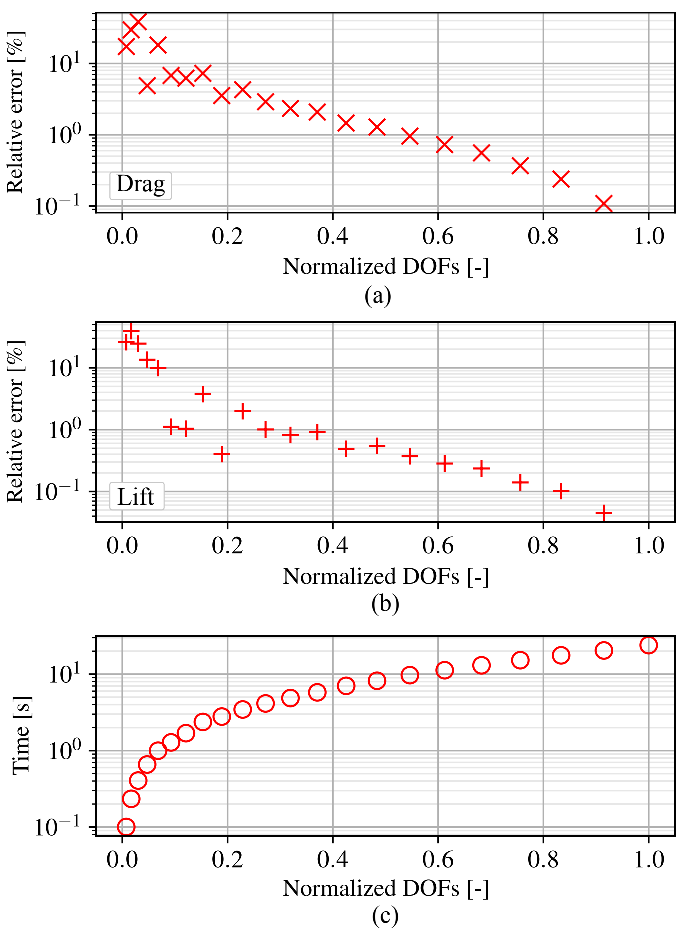

Fig. 4. Comparison of the computation time and accuracy varying with the discretization of the PEEC model. (a) Relative error of the drag force. (b) Relative error of the lift force. (c) Computation time.

PEEC and 3-D FEM is therefore conducted with the track represented in Fig. 1, and the parameters listed in Table I. The holes are introduced by setting the resistivity of the corresponding elements to a very high value, chosen here to be three orders of magnitude higher than that of the track. That value, impacting both the precision of the model but also its convergence and computation time, is chosen as a good trade-off between the two. In Fig. 5, the evolution of the forces as a function of the position of the PMs with respect to the track, computed using the PEEC model and time-dependent FEM, is depicted. The close agreement between them demonstrates the accuracy of the PEEC model, with a maximum error below 3 %. With holes in the track, the validity of the hypothesis linked to the z-component of the eddy currents may not hold. The FEM model was therefore also evaluated under the assumption that there is no vertical eddy current, aligning with the assumptions of the PEEC model. It can be seen that the FEM results are closer to the PEEC estimation, although the deviation due to this hypothesis is not that significant. The slight remaining difference in the lift force could be reduced with a refinement of the mesh in the FEM model, but the latter already took more than 12 hours to obtain the solution.

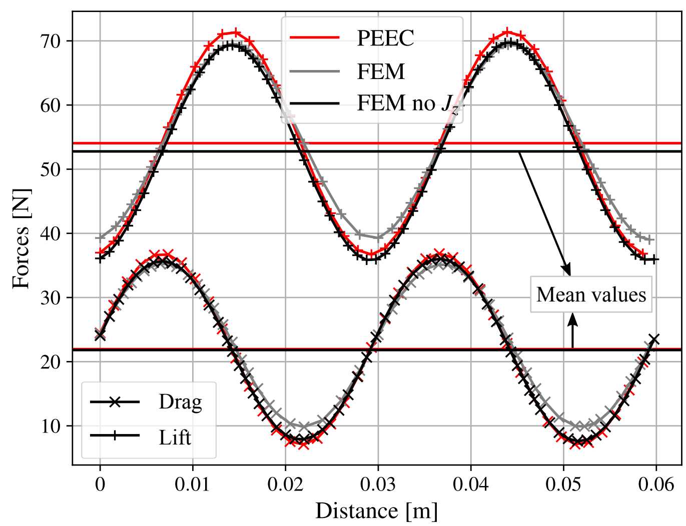

Fig. 5. Evolution of the forces with the relative position between the PMs and the perforated track, computed using PEEC and FEM.

The computation time of the PEEC is compared to that of the other models in Table II. For the bulk track, the analytical model is obviously the fastest since no discretization is introduced by the model. In contrast, when the track is perforated, only time-dependent FEM (FEM t-d) can model the system but at a high computational cost, while the computation time of the PEEC model remains the same as in the bulk case.

C. Experimental validation

An experimental setup, shown in Fig. 6, has been built to characterize small-scale electrodynamic suspensions. An annular aluminum track with a mean radius of 0.43 m is driven by a motor and rotates with respect to fixed permanent

TABLE II
COMPARISON THE COMPUTATION TIME OF THE DIFFERENT MODELS

Model	Analytical	FEM t-d	PEEC
w/o holes [s]	< 0.1	1.6e4	10
w/ holes [s]	$\times$	$> 2e4$	10

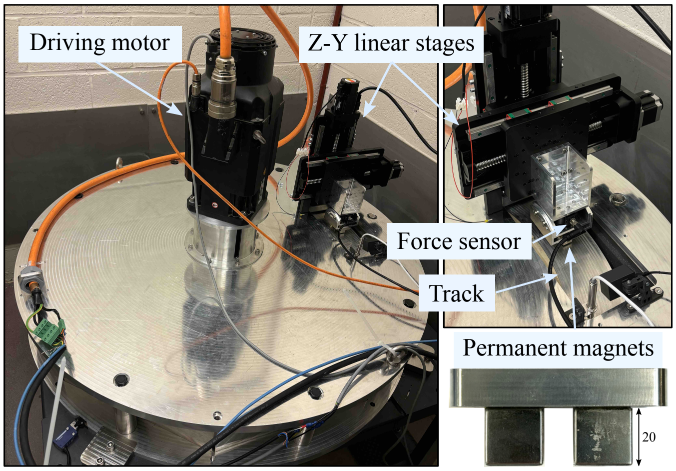

Fig. 6. Pictures of the rotary experimental setup.

TABLE III
CHARACTERISTICS OF THE EXPERIMENTAL SETUP

Parameter	Value	Unit
Track inner radius	380	mm
Track outer radius	480	mm
Track thickness	10	mm
Track conductivity	2.5e7	S/m
Air gap thickness	5	mm
PM thickness	20	mm
PM width	20	mm
PM length	20	mm
PM gap	10	mm
PM remanence	1.32	T

magnets, precisely positioned thanks to linear stages. By neglecting the curvature of the track, the behavior of the magnetic suspension can be emulated. The PM arrangement is made of two PMs with the same dimensions as for the numerical validation. The main characteristics and parameters of the setup are listed in Table III.

The forces, measured by a 6-axis force sensor for different speeds, are compared with the prediction of the PEEC model in Fig. 7. It can be seen that the model is able to calculate the forces in the system over all speeds, meaning that the skin effect in the track is well modeled. At 45 m/s, the skin depth is indeed equal to a third of the track thickness. The discrepancies, around $4\ \%$ on the lift force and $10\ \%$ on the drag force at 45 m/s, can be attributed to the end effects since the present implementation of the PEEC model considers a periodic repetition of the PM arrangement ($L_x = 2\tau_m$) whereas only two PMs are mounted in the experimental setup.

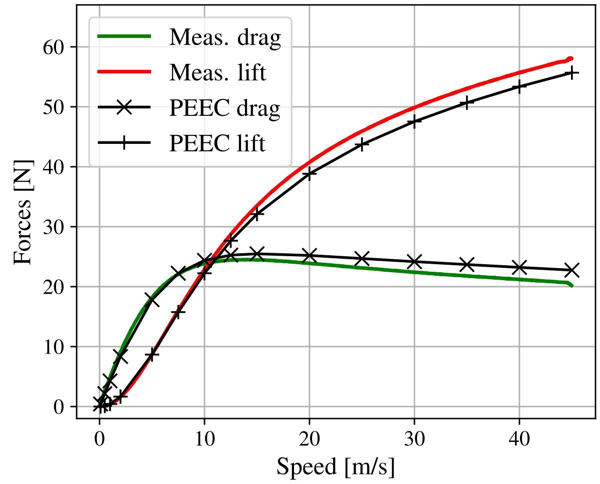

Fig. 7. Comparison of the measured and simulated forces generated by the suspension as a function of the speed.

IV. DYNAMIC MODEL

This section shows how the PEEC model can be adapted to study the vertical dynamics and stability of the suspension, without requiring additional FEM simulations. The model is then applied to a brief dynamic study.

A. Derivation

Faraday's law in each loop is written, in the time domain, as:

$$\mathbf{\Lambda R \Lambda}^T \mathbf{I} + \mathbf{\Lambda L \Lambda}^T \frac{d\mathbf{I}}{dt} = -\frac{d\boldsymbol{\varphi}}{dt} \tag{16}$$

where the resistance, inductance and incidence matrices $\mathbf{R}$, $\mathbf{L}$ and $\mathbf{\Lambda}$ respectively are the same as in the steady-state model. By defining $\mathbf{R}^\star = \mathbf{\Lambda R \Lambda}^T$ and $\mathbf{L}^\star = \mathbf{\Lambda L \Lambda}^T$, we have:

$$\mathbf{R}^\star \mathbf{I} + \mathbf{L}^\star \frac{d\mathbf{I}}{dt} = -\frac{d\boldsymbol{\varphi}}{dt} \tag{17}$$

The currents can be expressed as a sum of harmonic components:

$$\mathbf{I} = \sum_{n=1}^{N} \bar{\mathbf{I}}_n e^{j\omega_n t} \tag{18}$$

The same can be done for the loop fluxes:

$$\boldsymbol{\varphi} = \sum_{n=1}^{N} \boldsymbol{\varphi_{n,0}} e^{j\omega_n t} e^{j\omega_n \boldsymbol{\delta}/v_x} \tag{19}$$

where $(\boldsymbol{\varphi}_{n,0})_i$ has the same expression as in (12), and:

$$(\boldsymbol{\delta})_i = (i+1)\frac{L_x}{N_x} \tag{20}$$

By injecting (18) and (19) in (17) and assuming a steady-state in the x-direction, we have, for each harmonic:

$$\mathbf{R}^\star \bar{\mathbf{I}}_n + j\omega_n \mathbf{L}^\star \bar{\mathbf{I}}_n + \mathbf{L}^\star \frac{d\bar{\mathbf{I}}_n}{dt} + \left(\dot{z} \frac{\partial \boldsymbol{\varphi}_{n,0}}{\partial z} + j\omega_n \boldsymbol{\varphi}_{n,0} \right) e^{j\omega_n \boldsymbol{\delta}/v_x} = 0 \quad (21)$$

Finally, the following mechanical equation can be derived:

$$m\ddot{z} = F_z - F_p = \sum_n \mathrm{Re} \left[\frac{1}{2} \bar{\mathbf{I}}_n^T \left(\frac{\partial \boldsymbol{\varphi}_{n,0}}{\partial z} e^{j\omega_n \boldsymbol{\delta}/v_x} \right)^* \right] - F_p \quad (22)$$

with F_p and m the weight and the mass of the suspended system respectively. The complex currents $\bar{\mathbf{I}}_n$ can be separated into two real components $\bar{\mathbf{I}}_{n,d}$ and $\bar{\mathbf{I}}_{n,q}$, in such a way that:

$$\bar{\mathbf{I}}_n = \bar{\mathbf{I}}_{n,d} + j\bar{\mathbf{I}}_{n,q} \quad (23)$$

Three real equations can be thus obtained:

$$\mathbf{L}^\star \frac{d\bar{\mathbf{I}}_{n,d}}{dt} = -\mathbf{R}^\star \bar{\mathbf{I}}_{n,d} + \mathbf{L}^\star \omega_n \bar{\mathbf{I}}_{n,q} - \dot{z} \frac{\partial \boldsymbol{\varphi}_{n,0}}{\partial z} \cos(\omega_n \boldsymbol{\delta}/v_x) + \omega_n \boldsymbol{\varphi}_{n,0} \sin(\omega_n \boldsymbol{\delta}/v_x) \quad (24)$$

$$\mathbf{L}^\star \frac{d\bar{\mathbf{I}}_{n,q}}{dt} = -\mathbf{R}^\star \bar{\mathbf{I}}_{n,q} - \mathbf{L}^\star \omega_n \bar{\mathbf{I}}_{n,d} - \dot{z} \frac{\partial \boldsymbol{\varphi}_{n,0}}{\partial z} \sin(\omega_n \boldsymbol{\delta}/v_x) - \omega_n \boldsymbol{\varphi}_{n,0} \cos(\omega_n \boldsymbol{\delta}/v_x) \quad (25)$$

$$m\ddot{z} = \sum_n \frac{1}{2} \left[\bar{\mathbf{I}}_{n,d}^T \frac{\partial \boldsymbol{\varphi}_{n,0}}{\partial z} \cos(\omega_n \boldsymbol{\delta}/v_x) + \bar{\mathbf{I}}_{n,q}^T \frac{\partial \boldsymbol{\varphi}_{n,0}}{\partial z} \sin(\omega_n \boldsymbol{\delta}/v_x) \right] - F_p \quad (26)$$

Equations (24)-(26) constitute a state-space model:

$$\dot{\mathbf{x}} = \mathbf{f}(\mathbf{x}) \quad (27)$$

where the state variables are:

$$\mathbf{x} = \begin{bmatrix} z & \dot{z} & \bar{\mathbf{I}}_{n,d}^T & \bar{\mathbf{I}}_{n,q}^T \end{bmatrix}^T \quad (28)$$

The system (27) can be integrated over time to obtain the dynamic response of the suspension.

In order to perform classical stability analyses around an operating point $\mathbf{x}_{eq}$, where the lift force balances the weight, the non-linear system (27) must be linearized in the following way:

$$\mathbf{f}(\mathbf{x}) = \mathbf{f}(\mathbf{x}_{eq}) + \frac{\partial \mathbf{f}}{\partial \mathbf{x}}(\mathbf{x}_{eq}) \cdot (\mathbf{x} - \mathbf{x}_{eq}), \quad (29)$$

The term $\frac{\partial \mathbf{f}}{\partial \mathbf{x}}(\mathbf{x}_{eq})$, referred as $\mathbf{A}_{lin}$, is the state matrix and its expression is given by:

$$\mathbf{A}_{lin} = \begin{bmatrix} 0 & 1 & \mathbf{0} & \mathbf{0} \\ (\mathbf{A}_{lin})_{1,0} & 0 & (\mathbf{A}_{lin})_{1,2} & (\mathbf{A}_{lin})_{1,3} \\ (\mathbf{A}_{lin})_{2,0} & (\mathbf{A}_{lin})_{2,1} & -\mathbf{L}^{\star -1}\mathbf{R}^\star & \omega_n \mathbf{E} \\ (\mathbf{A}_{lin})_{3,0} & (\mathbf{A}_{lin})_{3,1} & -\omega_n \mathbf{E} & -\mathbf{L}^{\star -1}\mathbf{R}^\star \end{bmatrix} \quad (30)$$

where $\mathbf{E}$ is an identity matrix, and:

$$(\mathbf{A}_{lin})_{1,0} = \frac{\bar{\mathbf{I}}_{n,d}^T \frac{\partial^2 \boldsymbol{\varphi}_{n,0}}{\partial^2 z} \cos(\omega_n \boldsymbol{\delta}/v_x)}{2m} \Big|_{eq} \quad (31)$$

$$+ \frac{\bar{\mathbf{I}}_{n,q}^T \frac{\partial^2 \boldsymbol{\varphi}_{n,0}}{\partial^2 z} \sin(\omega_n \boldsymbol{\delta}/v_x)}{2m} \Big|_{eq} \quad (32)$$

$$(\mathbf{A}_{lin})_{1,2} = \frac{\frac{\partial \boldsymbol{\varphi}_{n,0}}{\partial z}\Big|_{eq} \cos(\omega_n \boldsymbol{\delta}/v_x)}{2m} \quad (33)$$

$$(\mathbf{A}_{lin})_{1,3} = \frac{\frac{\partial \boldsymbol{\varphi}_{n,0}}{\partial z}\Big|_{eq} \sin(\omega_n \boldsymbol{\delta}/v_x)}{2m} \quad (34)$$

$$(\mathbf{A}_{lin})_{2,0} = -\omega_n \mathbf{L}^{\star -1} \frac{\partial \boldsymbol{\varphi}_{n,0}}{\partial z}\Big|_{eq} \sin(\omega_n \boldsymbol{\delta}/v_x) \quad (35)$$

$$(\mathbf{A}_{lin})_{2,1} = -\omega_n \mathbf{L}^{\star -1} \frac{\partial \boldsymbol{\varphi}_{n,0}}{\partial z}\Big|_{eq} \cos(\omega_n \boldsymbol{\delta}/v_x) \quad (36)$$

$$(\mathbf{A}_{lin})_{3,0} = \omega_n \mathbf{L}^{\star -1} \frac{\partial \boldsymbol{\varphi}_{n,0}}{\partial z}\Big|_{eq} \cos(\omega_n \boldsymbol{\delta}/v_x) \quad (37)$$

$$(\mathbf{A}_{lin})_{3,1} = -\omega_n \mathbf{L}^{\star -1} \frac{\partial \boldsymbol{\varphi}_{n,0}}{\partial z}\Big|_{eq} \sin(\omega_n \boldsymbol{\delta}/v_x) \quad (38)$$

B. Dynamic study

With the dynamic system now established, its capability to capture the vertical dynamics of the suspension is demonstrated through a case study. In Fig 8, a disturbance of 5% of the equilibrium air gap (20 mm) is applied to the system at 50 m/s. It is shown that the evolution of the air gap over time is well estimated using the linearized dynamic model compared to the non-linear one.

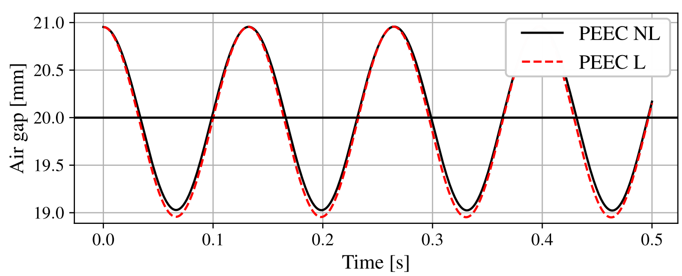

Fig. 8. Evolution of the forces with the vertical position between the PMs and the continuous track, computed using the non-linear (NL) and linearized (L) dynamic PEEC models. The horizontal black line represents the equilibrium air gap.

To investigate the vertical stability of the system, a root locus analysis is performed on the linearized model by varying the speed of the suspension in the x-direction. Fig. 9 depicts the mechanical poles on the right and the first two electrical poles on the left. Each current loop in the dynamic model introduces a pair of complex conjugate electrical poles, but since they are far from the imaginary axis, they are omitted from the figure. The mechanical behavior of the suspension is influenced by its forward speed. Fig. 10 presents the response of the linearized system at key points, indicated by a cross in the root locus in Fig. 9, showing how the real and imaginary parts of the mechanical poles evolve with speed. It can be seen that the system becomes unstable above a given forward speed, with the mechanical poles crossing the imaginary axis.

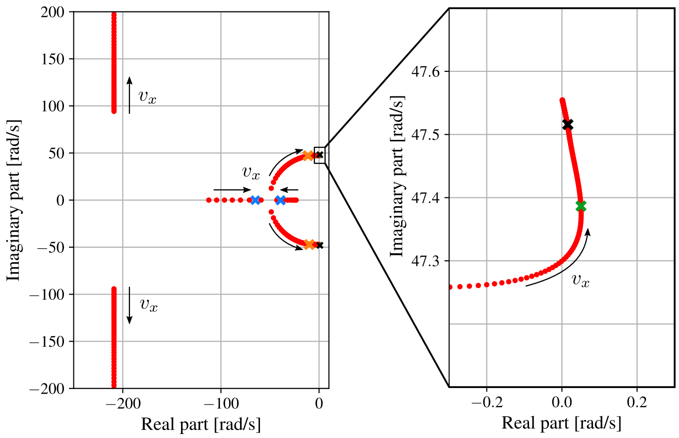

Fig. 9. The mechanical poles and the first electrical poles of the root locus (left) and a zoom on the crossing of the imaginary axis (right).

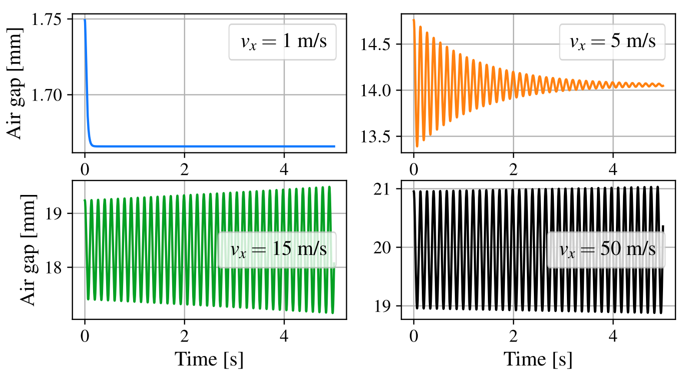

Fig. 10. Dynamic response of the system to a 5% perturbation of the air gap for different speeds, indicating by a cross in Fig. 9.

V. Conclusion

This paper presented a PEEC model to study PM-EDSs in 3-D. Using a network of interconnected conductive elements forming equivalent circuits, the forces generated by the suspension can be accurately computed, while considering the skin effect and with no apriori knowledge of the eddy current pattern. Through its application to a case study, it was shown that it is particularly well suited to model track topologies presenting holes, usually requiring computationally intensive FEM simulations. Coupled with mechanical equations, the model can also be adapted to study the vertical dynamic behavior of the suspension, without relying on any FEM identification.

Acknowledgment

The authors would like to thank the CREDEM platform for the construction of the experimental setup. In addition, they would also like to recognize the work of Thomas Derneden as a first step towards the elaboration of the model.

References

[1] L. Beauloye and B. Dehez, “Permanent magnet electrodynamic suspensions applied to maglev transportation systems: A review,” *IEEE Transactions on Transportation Electrification*, vol. 9, no. 1, pp. 748–758, 2022.

[2] C. Wu, G. Li, D. Wang, and J. Xu, “An efficient analytical model and experiments of 3d electromagnetic force of permanent magnet electrodynamic suspension system,” *Journal of Applied Physics*, vol. 132, no. 17, p. 175001, Nov. 2022.

[3] Y. Chen, W. Zhang, J. Z. Bird, S. Paul, and K. Zhang, “A 3-d analytic-based model of a null-flux halbach array electrodynamic suspension device,” *IEEE Transactions on Magnetics*, vol. 51, no. 11, p. 1–5, Nov. 2015.

[4] L. Beauloye and B. Dehez, “Comparison of track topologies of permanent magnet electrodynamic suspensions,” in *2023 14th International Symposium on Linear Drivers for Industry Applications (LDIA)*, 2023, pp. 1–5.

[5] B.-T. Ooi, “A dynamic circuit theory of the repulsive magnetic levitation system,” *IEEE Transactions on Power Apparatus and Systems*, vol. 96, no. 4, pp. 1094–1100, 1977.

[6] J. L. He, D. Rote, and H. Coffey, “Applications of the dynamic circuit theory to maglev suspension systems,” *IEEE Transactions on Magnetics*, vol. 29, no. 6, p. 4153–4164, Nov. 1993.

[7] R. Post and D. Ryutov, “The inductrack: a simpler approach to magnetic levitation,” *IEEE Transactions on Applied Superconductivity*, vol. 10, no. 1, p. 901–904, Mar. 2000.

[8] J. Bird, “An investigation into the use of electrodynamic wheels for high-speed ground transportation,” Ph.D. dissertation, University of Wisconsin–Madison, 2007.

[9] D. Rote and Y. Cai, “Review of dynamic stability of repulsive-force maglev suspension systems,” *IEEE Transactions on Magnetics*, vol. 38, no. 2, p. 1383–1390, Mar. 2002.

[10] N. Paudel and J. Z. Bird, “Modeling the dynamic electromechanical suspension behavior of an electrodynamic eddy current maglev device,” *Progress In Electromagnetics Research B*, vol. 49, p. 1–30, 2013.

[11] C. Wu, G. Li, D. Wang, and J. Xu, “Dynamic characterization of permanent magnet electrodynamic suspension system with a novel passive damping magnet scheme,” *Journal of Sound and Vibration*, vol. 599, p. 118849, Mar. 2025.

[12] R. Galluzzi, S. Circosta, N. Amati, A. Tonoli, A. Bonfitto, T. A. Lembke, and M. Kertész, “A multi-domain approach to the stabilization of electrodynamic levitation systems,” *Journal of Vibration and Acoustics*, vol. 142, no. 6, May 2020.

[13] E. Tramacere, M. Pakštys, R. Galluzzi, N. Amati, A. Tonoli, and T. A. Lembke, “Modeling and experimental validation of electrodynamic maglev systems,” *Journal of Sound and Vibration*, vol. 568, p. 117950, Jan. 2024.

[14] G. Antonini, A. E. Ruehli, D. Romano, and F. Loreto, “The Partial Elements Equivalent Circuit Method: The State of the Art,” *IEEE Transactions on Electromagnetic Compatibility*, vol. 65, no. 6, pp. 1695–1714, Dec. 2023.

[15] A. Ruehli, “Equivalent circuit models for three-dimensional multiconductor systems,” *IEEE Transactions on Microwave Theory and Techniques*, vol. 22, no. 3, p. 216–221, Mar. 1974.

[16] D. Romano and G. Antonini, “Partial Element Equivalent Circuit Formulation for Moving Objects,” *IEEE Transactions on Electromagnetic Compatibility*, vol. 61, no. 5, pp. 1586–1592, Oct. 2019.

[17] J. Liu, W. Li, L. Jin, G. Lin, Y. Sun, and Z. Zhang, “Analysis of linear eddy current brakes for maglev train using an equivalent circuit method,” *IET Electrical Systems in Transportation*, vol. 11, no. 3, pp. 218–226, Sep. 2021.

[18] S. Paul and J. Z. Bird, “A 3-D analytic eddy current model for a finite width conductive plate,” *COMPEL: The International Journal for Computation and Mathematics in Electrical and Electronic Engineering*, vol. 33, no. 1/2, pp. 688–706, Dec. 2013.

[19] C. Hoer and Y. Love, “Exact inductance equations for rectangular conductors with applications to more complicated geometries,” *Journal of Research of the National Bureau of Standards. C, Engineering and Instrumentation*, vol. 69, no. 2, pp. 127–137, 1965.

[20] F. W. Grover, *Inductance calculations: working formulas and tables*. Courier Corporation, 2004.

[21] C. Dumont de Chassart, M. Van Beneden, V. Kluyskens, and B. Dehez, "Semi-analytical determination of inductances in windings with axial and azimuthal wires," *COMPEL: The International Journal for Computation and Mathematics in Electrical and Electronic Engineering*, vol. 35, no. 1, pp. 2–15, 2016.

[22] J. Lim, C.-Y. Lee, Y. J. Oh, J.-M. Jo, J.-H. Lee, K.-S. Lee, and S. Choi, "Equivalent inductance model for the design analysis of electrodynamic suspension coils for hyperloop," *Scientific Reports*, vol. 11, no. 1, p. 23499, Dec. 2021.

[23] T. Lubin and A. Rezzoug, "3-D Analytical Model for Axial-Flux Eddy-Current Couplings and Brakes Under Steady-State Conditions," *IEEE Transactions on Magnetics*, vol. 51, no. 10, pp. 1–12, Oct. 2015.